Electronic Supplementary Material (ESI) for Journal of Materials Chemistry A.

Supplementary Information

Transforming bulk alloys into nanoporous lanthanum-based perovskite oxides with high specific surface areas and enhanced electrocatalytic activities

Conghui Si[a,d], Chi Zhang[b], Jaka Sunarso[c,*], Zhonghua Zhang[a,*]

[a] Key Laboratory for Liquid-Solid Structural Evolution and Processing of Materials (Ministry of Education), School of Materials Science and Engineering, Shandong University, Jinan 250061, China. Email: zh_zhang@sdu.edu.cn.

[b] School of Applied Physics and Materials, Wuyi University, Jiangmen 529020, Guangdong, China.

[c] Research Centre for Sustainable Technologies, Faculty of Engineering, Computing and Science, Swinburne University of Technology, Jalan Simpang Tiga, 93350, Kuching, Sarawak, Malaysia. Email: jsunarso@swinburne.edu.my.

[d] Key Laboratory of Processing and Testing Technology of Glass and Functional Ceramics of Shandong Province, School of Material Science and Engineering, Qilu University of Technology (Shandong Academy of Sciences), Jinan 250353, China.

Experimental section

Materials synthesis

Nanoporous $LaMO_3$ (M = Co, Mn, Ni, or Cr) perovskite oxides were synthesized *via* an innovative synthesis route, which includes de-alloying process followed by annealing. Firstly, the ternary alloys with nominal compositions of $Al_{88}La_6M_6$ (M = Co, Mn, Ni, or Cr) were synthesized by arc melting pure Al, La, and M (99.9 wt. %) under an argon atmosphere. In a typical procedure, pure Al, La and M (M = Co, Mn, Ni or Cr) were arc-melted under the protection of Ar atmosphere. The temperature of Al-La-M melt was kept at 900-1000 ℃. The Al-La-M ingots were repeatedly melted three-four times to obtain the alloys with homogeneous compositions. Subsequently, the alloy ingots were re-melted and rapidly solidified into foils through a melt spinning technique. The resulting alloy foils were about 2-4 mm in width and 20-50 μm in thickness. Then, the precursor alloy foils were added into a 2 M NaOH solution and de-alloyed at room temperature until no bubbles emerged to ensure the Al element was fully dissolved. The products were washed repeatedly with ultra-pure water (18.2 MΩ cm) and dehydrated alcohol, and then dried at 60 °C in vacuum oven overnight. Finally, the as-dealloyed samples were thoroughly grounded in an agate mortar and then annealed in air at 800 °C for 2 h.

Materials characterization

The XRD patterns were collected on an XD-3 diffractometer (Beijing Purkinje General Instrument Co., Ltd, China) using Cu-Kα radiation ($\lambda = 0.15406$ nm) at a 40 kV voltage and a 30 mA current. The microstructure and morphology of the samples were analyzed by SEM (FEI QUANTA FEG250) using a secondary electron mode at a 15 kV accelerating voltage. EDX analysis and mapping were performed using the FEI QUANTA FEG250 SEM equipped with an Oxford Instrument EDX spectrometer. The microstructure and crystal structure of the samples were characterized by TEM (JEOL JEM-2100). The surface compositions and the oxidation states were characterized by XPS (ESCALAB 250) using Al-Kα radiation excitation source, with all XPS spectra corrected using C 1s electron binding energy at 284.6 eV. BET specific surface area measurements were performed using N_2 adsorption-desorption on a Gold APP V-Sorb 2800P surface area and porosity analyzer at 77 K.

Electrochemical measurements

Working electrodes were fabricated by drop-coating catalyst ink on the polished GC electrode with a diameter of 5.0 mm (geometric surface area, 0.196 cm^2). The catalyst ink was a mixture of 5.0 mg of synthesized sample, 5.0 mg of XC-72 carbon powder, and 0.5 mL of Nafion solution (0.5 wt. %) dispersed in 1.5 mL of isopropanol solvent. To form a homogeneous dispersion, the catalyst ink was ultrasonically treated for 0.5 h. 30 μL of the ink was then transferred onto the GC electrode and dried in a vacuum tank at room temperature for at least 3 h, yielding a catalyst mass loading of 0.30 $mg_{catalyst}$ cm^{-2}. As a control reference, commercial Pt/C (40 wt.% Pt, Johnson Matthey) with a loading of 0.05 mg_{Pt} cm^{-2} was also utilised.

Electrochemical measurements were performed on a CHI 760E potentiostat with a

RDE system to evaluate the electrocatalytic performance of the catalysts. A standard three-electrode cell was performed using saturated calomel electrode (SCE) as the reference electrode, a bright Pt plate as the counter electrode, and sample modified GC electrode as the working electrode. For the ORR and OER tests, the polarization curves were recorded in an O_2-saturated 0.1 M or 1.0 M KOH electrolyte, which was prepared using de-ionized water (>18 MΩ cm). O_2 was bubbled into the electrolyte to ensure the O_2/H_2O equilibrium at 1.23 V vs. RHE. The working electrodes were scanned at various rotation rates from 400 to 2500 rpm at a 10 mV s^{-1} scan rate to evaluate the ORR performance. Electrochemical impedance spectra were conducted on an impedance analyzer (ZAHNER Zennium) with a frequency range of 10 mHz to 100 kHz at a potential of 0.65 V vs. RHE. The ORR durability testing was performed under half-cell conditions in a 0.1 M KOH electrolyte. The chronopotentiometry test for OER was conducted at a constant current density of 10 mA cm^{-2} for 10000 s. The working electrode was cycled from -0.8 to 0.1 V vs. SCE at a 50 mV s^{-1} scan rate and the ORR durability was tested by performing LSVs after 10,000 cycles. To evaluate the methanol tolerance of the catalysts during ORR, the polarization curves were also obtained in a 0.1 M KOH electrolyte upon introducing a 0.1 M MeOH or a 0.5 M MeOH solution at 1600 rpm and 10 mV s^{-1}. Additionally, RRDE measurements were performed during ORR at 10 mV s^{-1} in the O_2-saturated 0.1 M KOH solution at room temperature. The ring potential was maintained at 1.3 V vs. RHE, which was considered to be sufficiently high to induce complete peroxide decomposition. The hydrogen peroxide yield in $\%(H_2O_2)$ and electron transfer number n were determined using the following equations:

$$\% (H_2O_2) = 200I_{ring}/(I_{disk}N + I_{ring}) \quad (1)$$

$$n = 4I_{disk}N/(I_{disk}N + I_{ring}) \quad (2)$$

where I_{ring} is the ring current, I_{disk} is the disk current, and N is the current collection efficiency of the Pt ring. N was determined to be 0.37 from the reduction of $K_3Fe[CN]_6$.

DFT calculations

DFT calculations were performed with the CASTEP simulation package in Materials Studio (version 7.0) of Accelrys Inc. The Perdew-Burke-Ernzerhof (PBE) function was used in the generalized gradient approximation (GGA) calculation, and a cut-off energy of 300 eV was used for the plane wave truncation. The Brillouin zone was presented by Monkhorst-Pack k-point meshes of 2×3×1 for all the calculations. The structure of perovskite-type $LaMO_3$ is shown in **Fig. S23** and a periodic-slab approach was used to represent the (001) plane of $LaMO_3$. A vacuum region of around 15 Å was employed along the z-direction to avoid the interaction between the neighboring molecules. The two bottom layers of the slab were fixed and the top layer was allowed to relax. The self-consistent field convergence criterion was set to be an energy change of 10^{-6} eV atom^{-1}. Different adsorption sites (top and bridge) were calculated and the adsorption energies (E_{ads}) of molecules for both surfaces were obtained using the following equation:

$$E_{ads} = E_{adsorbate} + E_{substrate} - E_{adsorbate/substrate} \quad (3)$$

where $E_{adsorbate}$ and $E_{substrate}$ represent the energy of the isolated adsorbate and substrate, respectively. $E_{adsorbate/substrate}$ represents the total energy of adsorbate/substrate system.

A positive value of E_{ads} corresponds to an exothermic process, which indicates that the adsorbate molecule can be easily adsorbed to the surface of the substrate.

Supplementary Figures

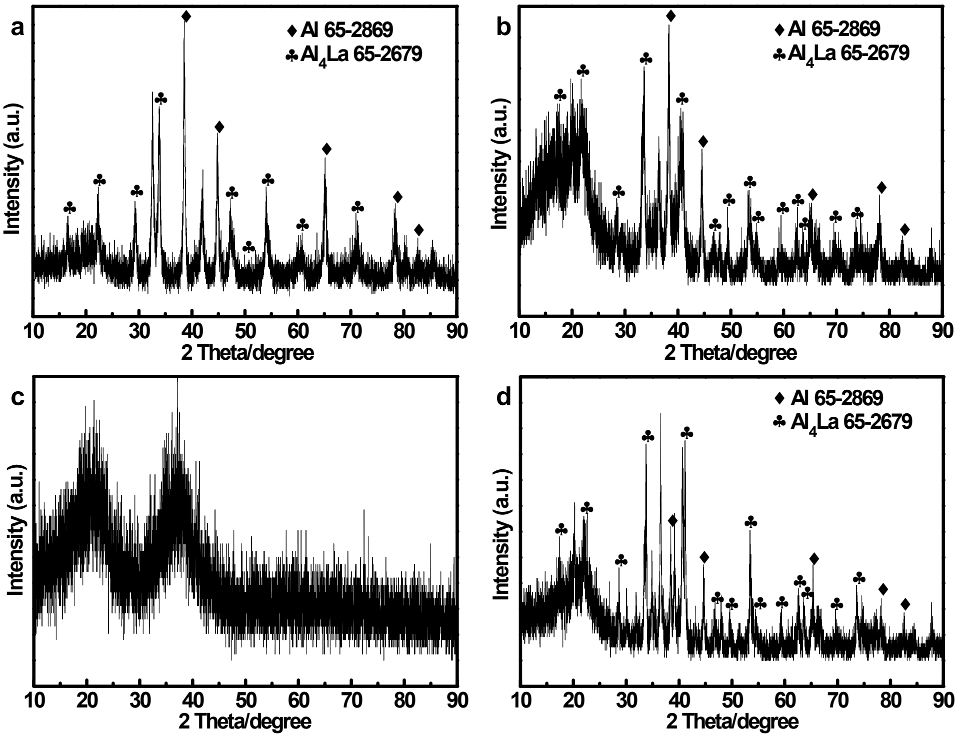

Figure S1. XRD patterns of the (**a**) $Al_{88}La_6Co_6$, (**b**) $Al_{88}La_6Mn_6$, (**c**) $Al_{88}La_6Ni_6$, and (**d**) $Al_{88}La_6Cr_6$ precursor foils. The XRD results indicate that the $Al_{88}La_6M_6$ (M = Co, Mn, or Cr) precursors mainly consist of two phases: Al (JCPDS 65-2869) and Al_4La (JCPDS 65-2679). It is reasonable to assume that M (= Co, Mn, or Cr) substitutes for partial La to form $Al_4(La,M)$. The rapidly solidified $Al_{88}La_6Ni_6$ precursor is composed of an amorphous phase.

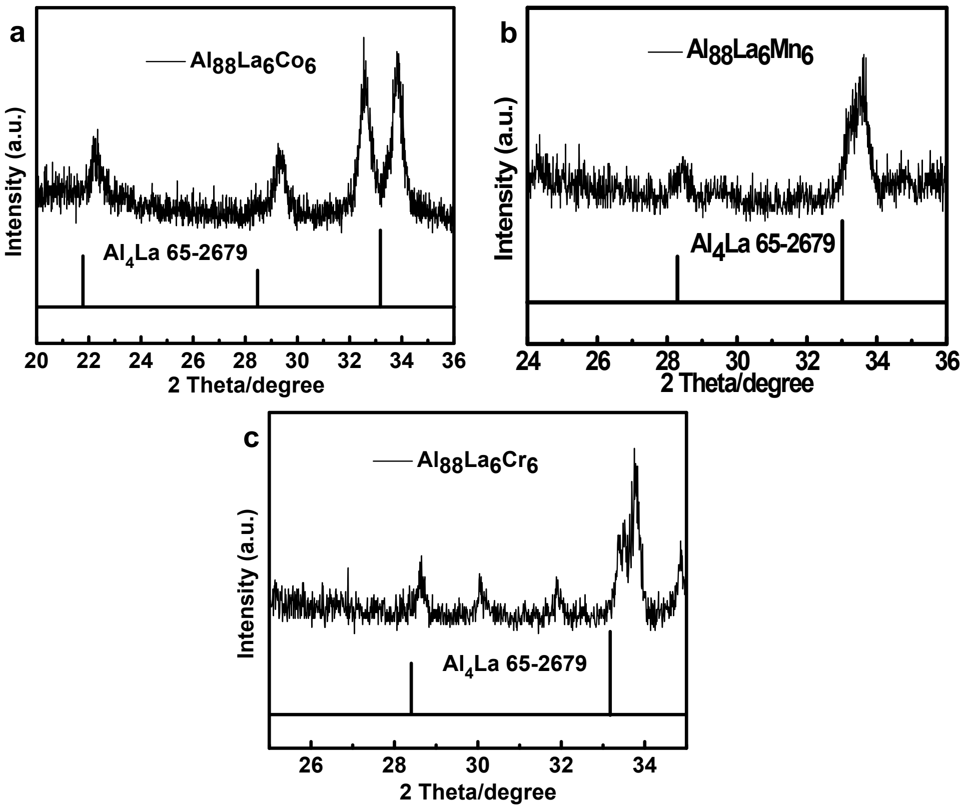

Figure S2. The enlarged parts of the XRD patterns for the (**a**) $Al_{88}La_6Co_6$, (**b**) $Al_{88}La_6Mn_6$, and (**c**) $Al_{88}La_6Cr_6$ precursor foils. Compared to the standard profile of Al_4La (JCPDS 65-2679), the diffraction peaks of $Al_4(La,M)$ shift positively owing to the substitution of M (M = Co, Mn or Cr) for La. Since the atomic radius of Co (0.126 nm), Mn (0.132 nm), and Cr (0.127 nm) is smaller than that of La (0.187 nm), lattice contraction might occur in $Al_4(La,M)$.

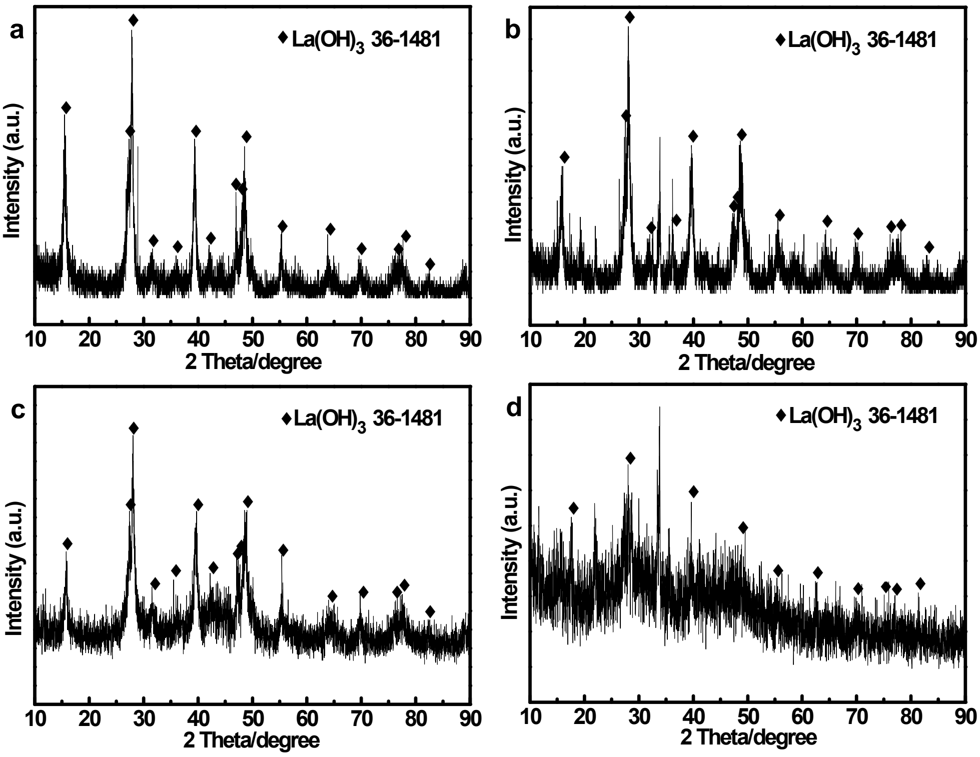

Figure S3. XRD patterns of the as-dealloyed samples: (**a**) (La,Co)$(OH)_3$, (**b**) (La,Mn)$(OH)_3$, (**c**) (La,Ni)$(OH)_3$, and (**d**) (La,Cr)$(OH)_3$. The M (M = Co, Mn, Ni, or Cr) elements are doped in the cationic sites of the bimetallic hydroxide (La,M)$(OH)_3$.

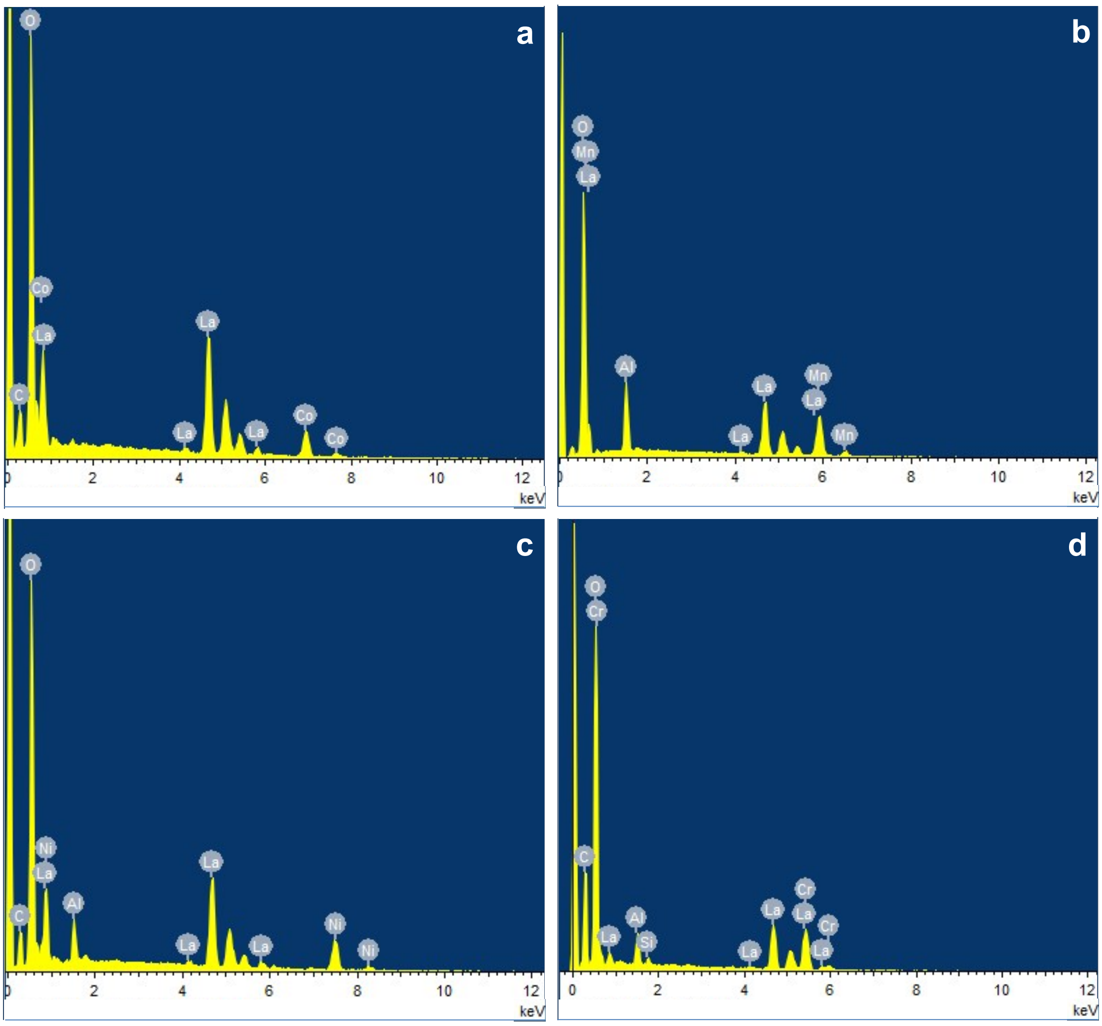

Figure S4. EDX spectra of the as-dealloyed samples: (**a**) (La,Co)$(OH)_3$, (**b**) (La,Mn)$(OH)_3$, (**c**) (La,Ni)$(OH)_3$, and (**d**) (La,Cr)$(OH)_3$. The EDX results further confirm the presence of M (M = Co, Mn, Ni, or Cr) elements and the atomic ratio of La: M is close to 1:1.

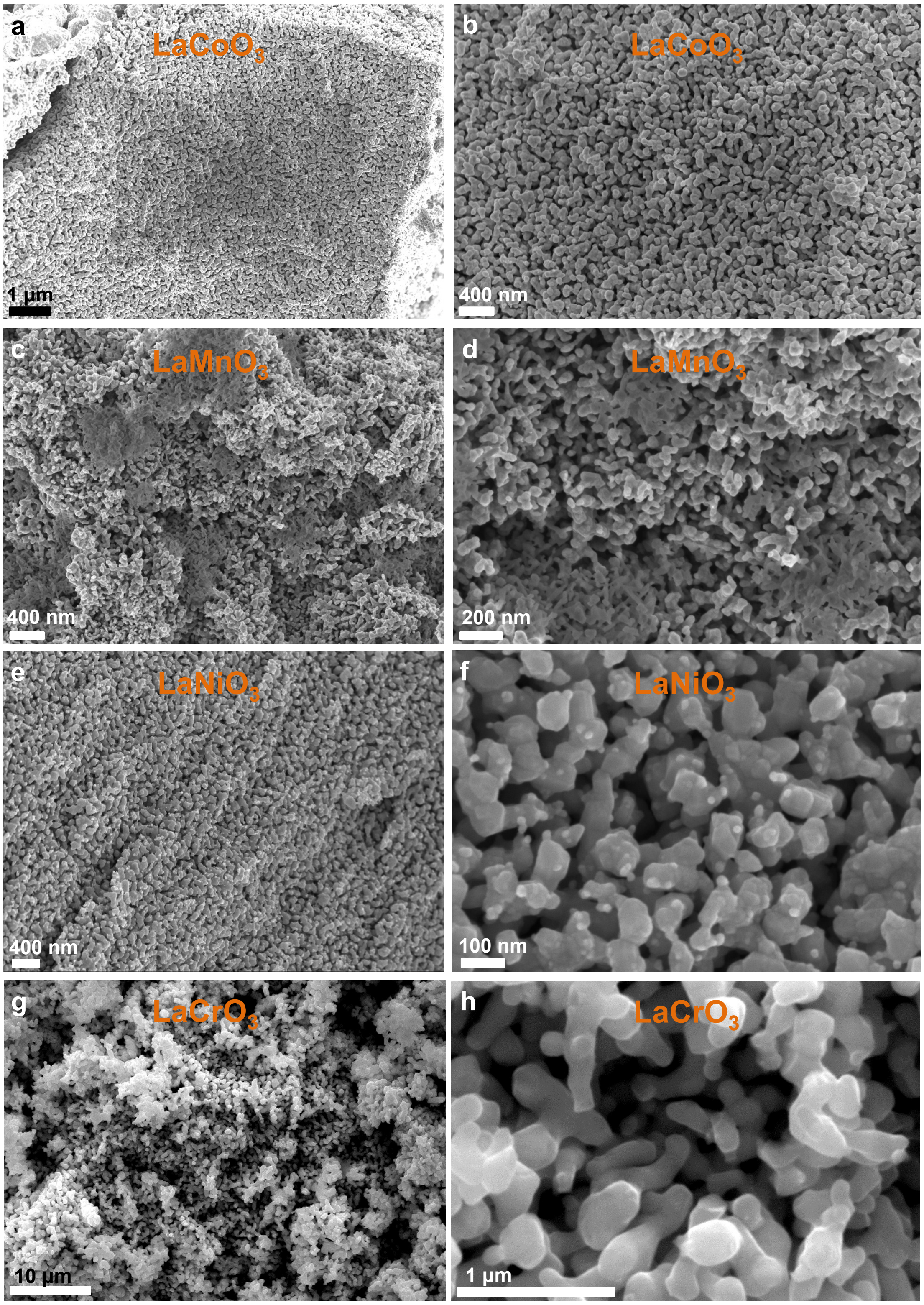

Figure S5. SEM images of the synthesized (**a,b**) $LaCoO_3$, (**c,d**) $LaMnO_3$, (**e,f**) $LaNiO_3$, and (**g,h**) $LaCrO_3$ samples.

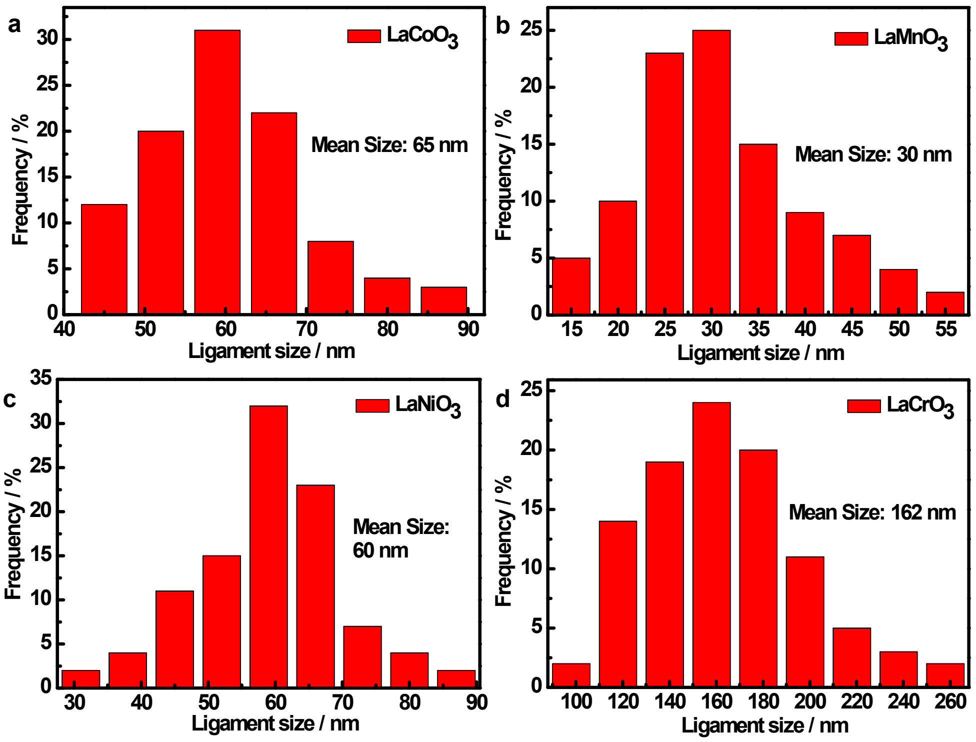

Figure S6. The ligament size distribution histograms of the (**a**) $LaCoO_3$, (**b**) $LaMnO_3$, (**c**) $LaNiO_3$, and (**d**) $LaCrO_3$ samples based on the SEM images in **Fig. 1c-f**. The mean ligament sizes are about 65, 30, 60, and 162 nm for the $LaCoO_3$, $LaMnO_3$, $LaNiO_3$, and $LaCrO_3$ samples, respectively.

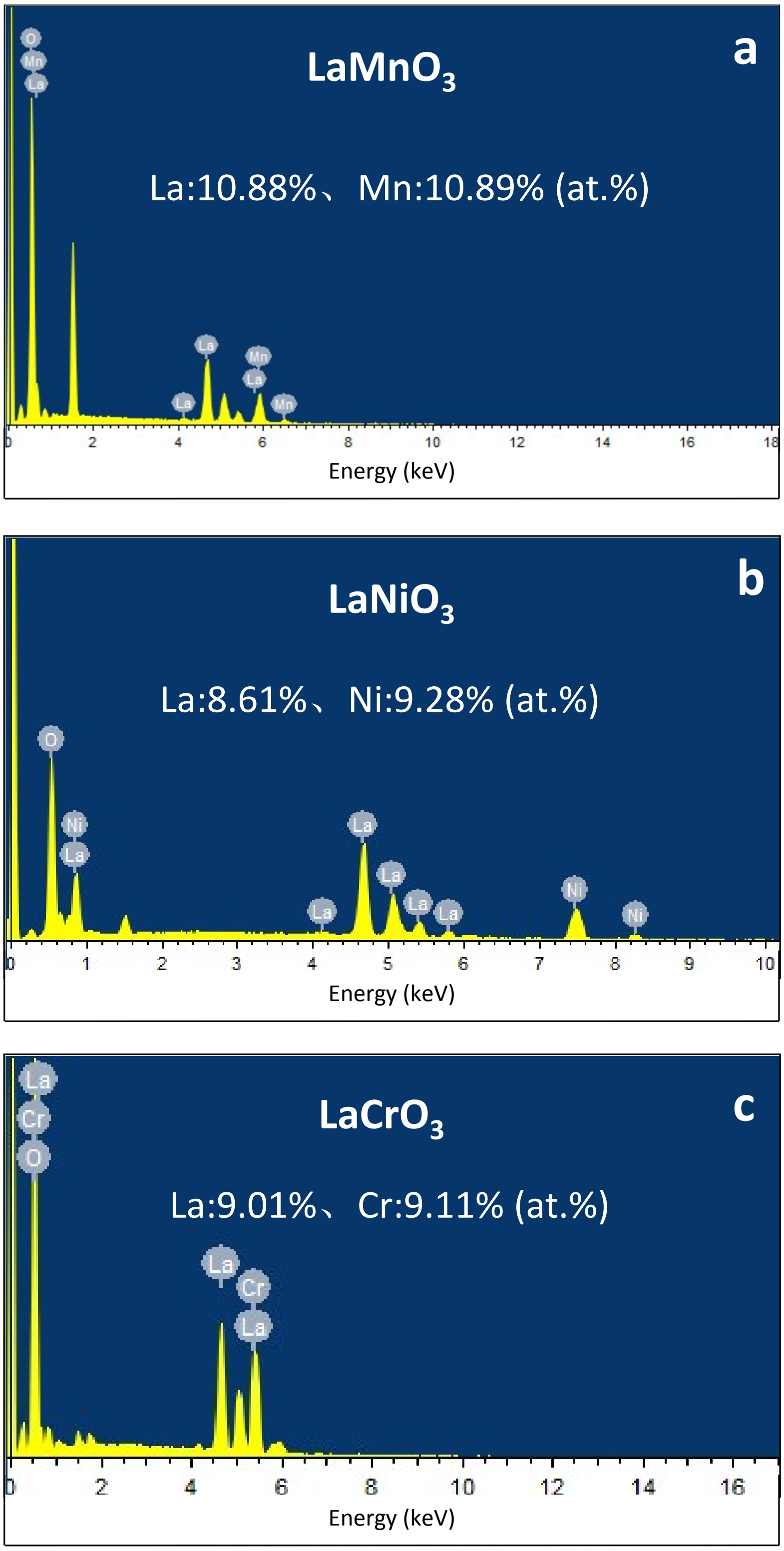

Figure S7. SEM-EDX spectra of the synthesized (**a**) LaMnO$_3$, (**b**) LaNiO$_3$, and (**c**) LaCrO$_3$ samples.

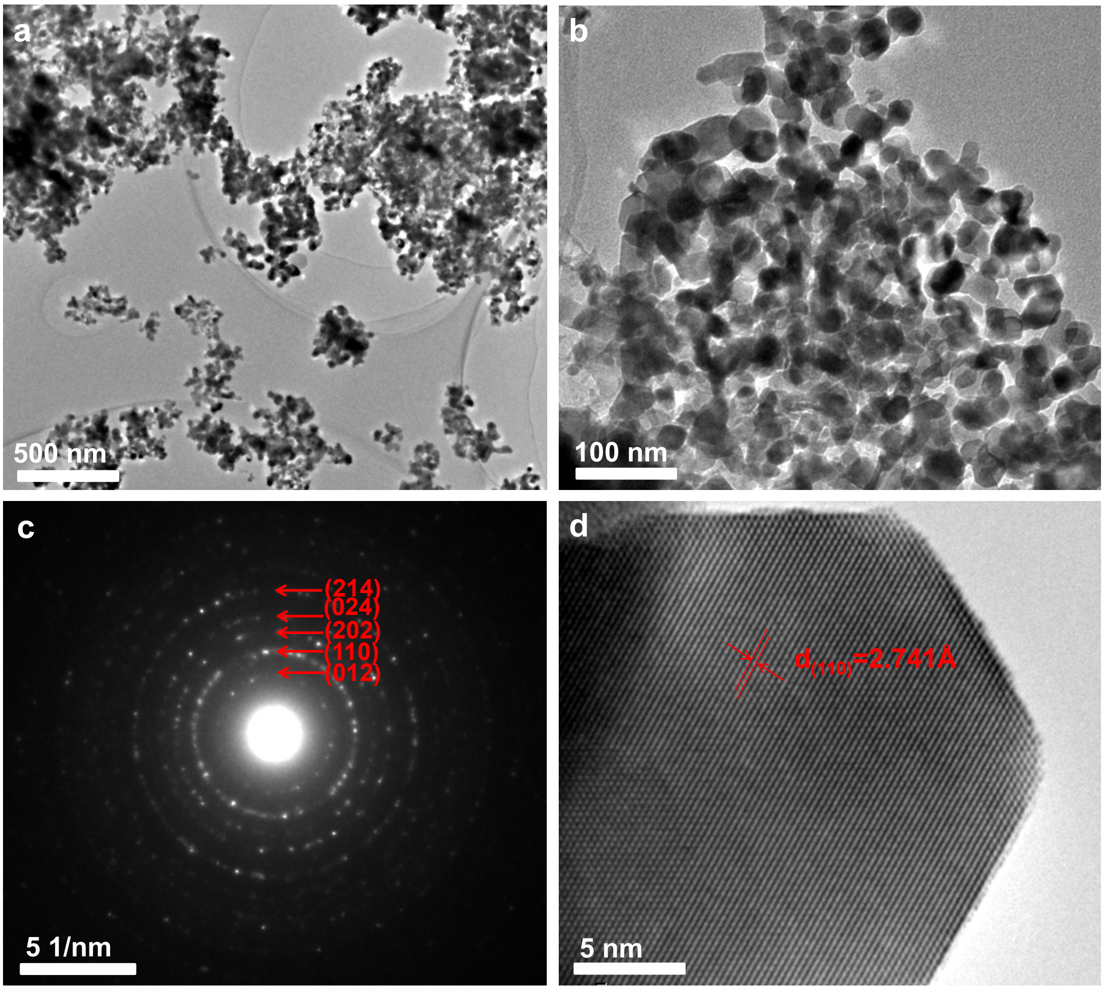

Figure S8. (**a,b**) TEM images, (**c**) SAED pattern, and (**d**) HRTEM image of the $LaMnO_3$ sample.

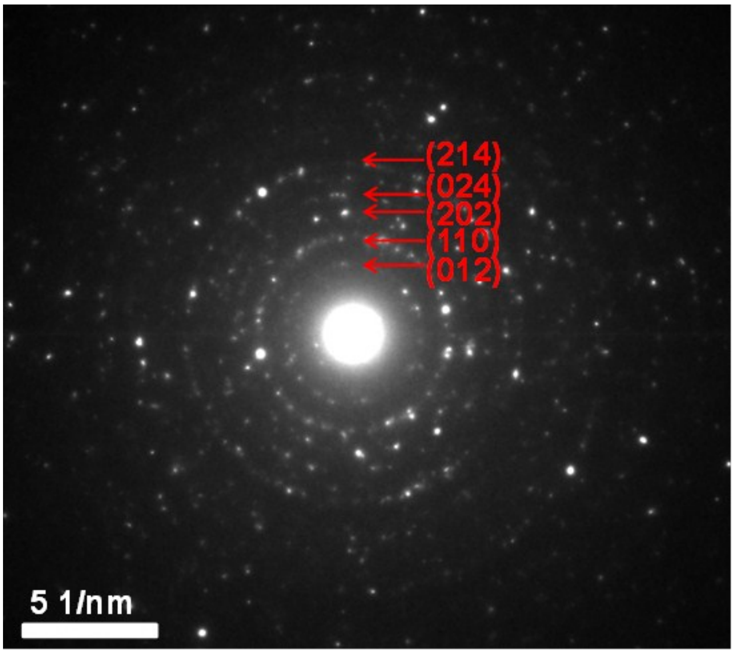

Figure S9. SAED pattern of the $LaCoO_3$ sample.

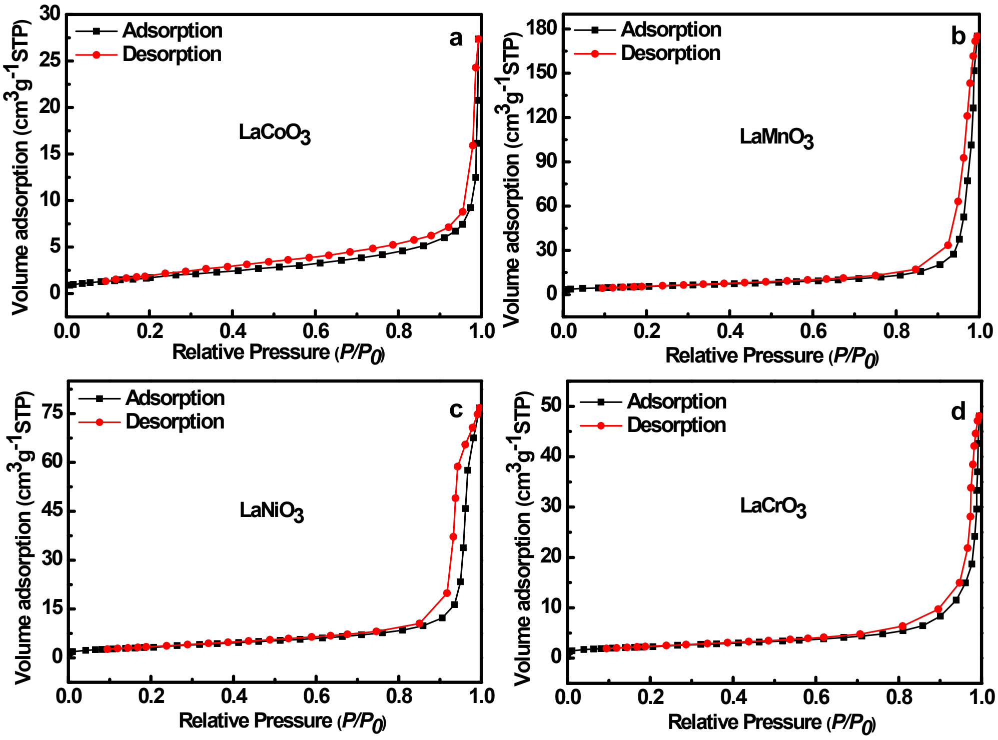

Figure S10. N_2 adsorption-desorption isotherms of the (**a**) $LaCoO_3$, (**b**) $LaMnO_3$, (**c**) $LaNiO_3$, and (**d**) $LaCrO_3$ samples.

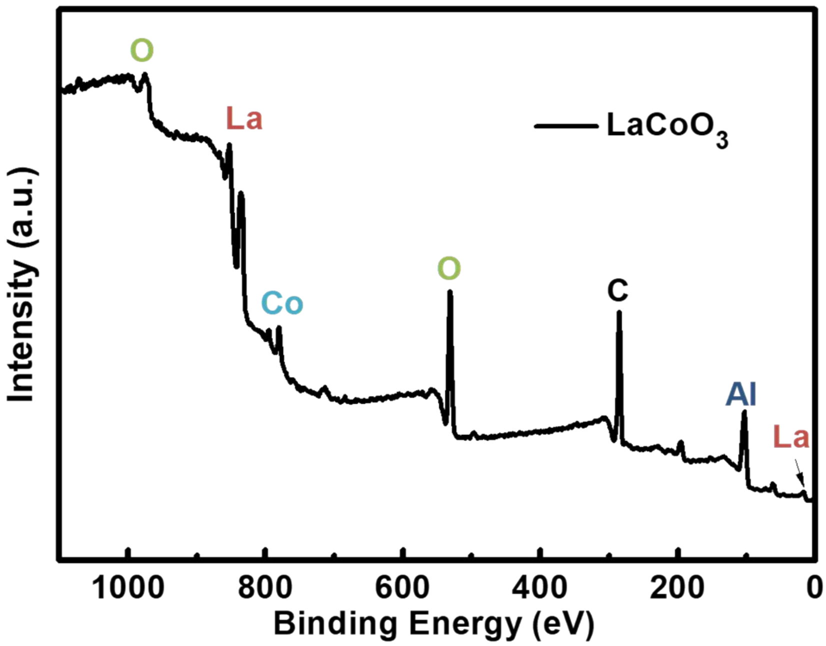

Figure S11. Total XPS spectrum of the LaCoO$_3$ sample. All spectra were calibrated using the adventitious C 1s peak with a fixed value of 284.6 eV.

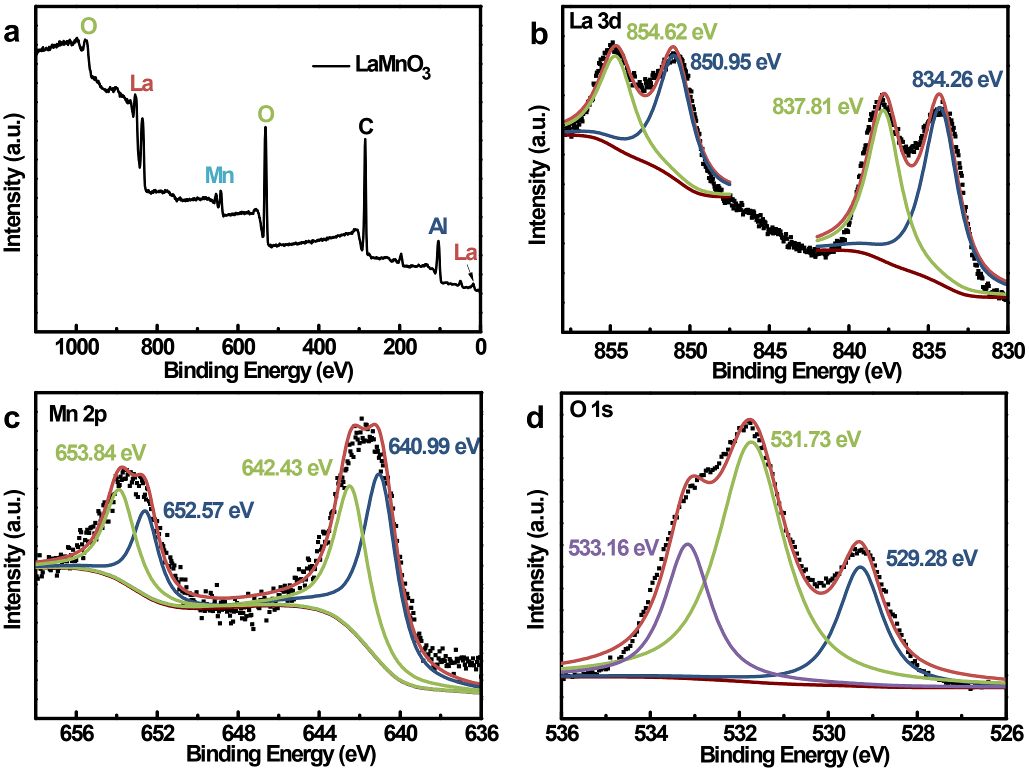

Figure S12. (**a**) Total XPS spectrum, (**b**) La 3d XPS spectrum, (**c**) Mn 2p XPS spectrum, and (**d**) O 1s XPS spectrum of the $LaMnO_3$ sample.

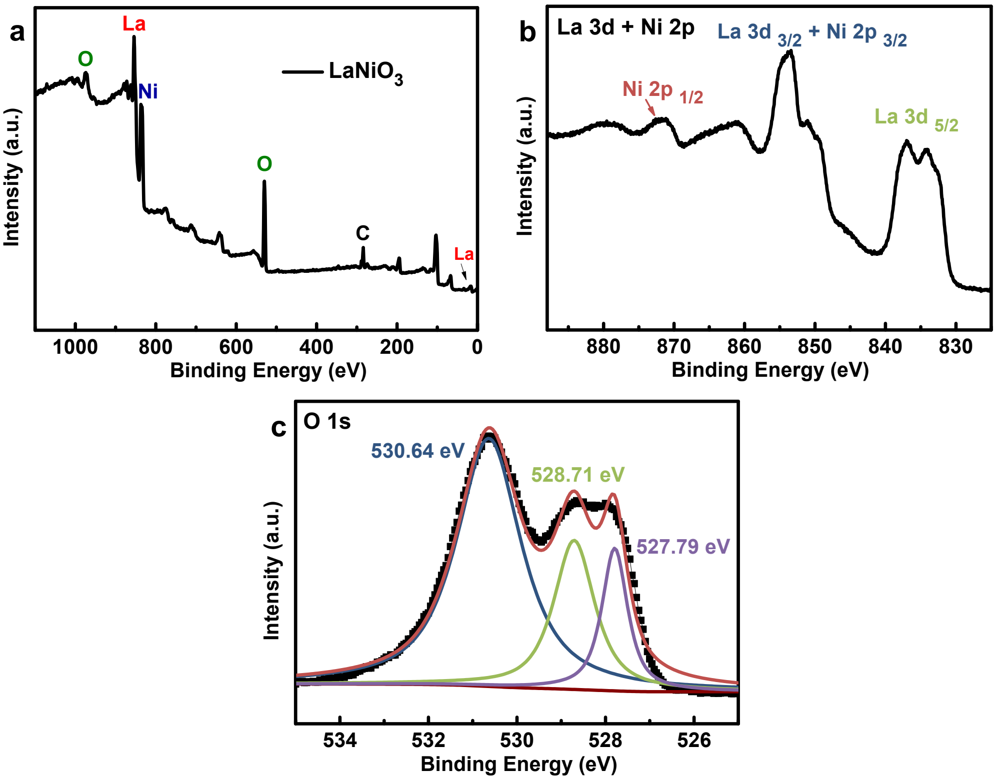

Figure S13. (**a**) Total XPS spectrum, (**b**) La 3d and Ni 2p XPS spectrum, and (**c**) O 1s XPS spectrum of the $LaNiO_3$ sample. It is known that the La $3d_{3/2}$ peak overlaps with the Ni $2p_{3/2}$ peak. Thus Ni $2p_{3/2}$ spectrum cannot be analyzed separately without the analysis of La $3d_{3/2}$ spectrum.

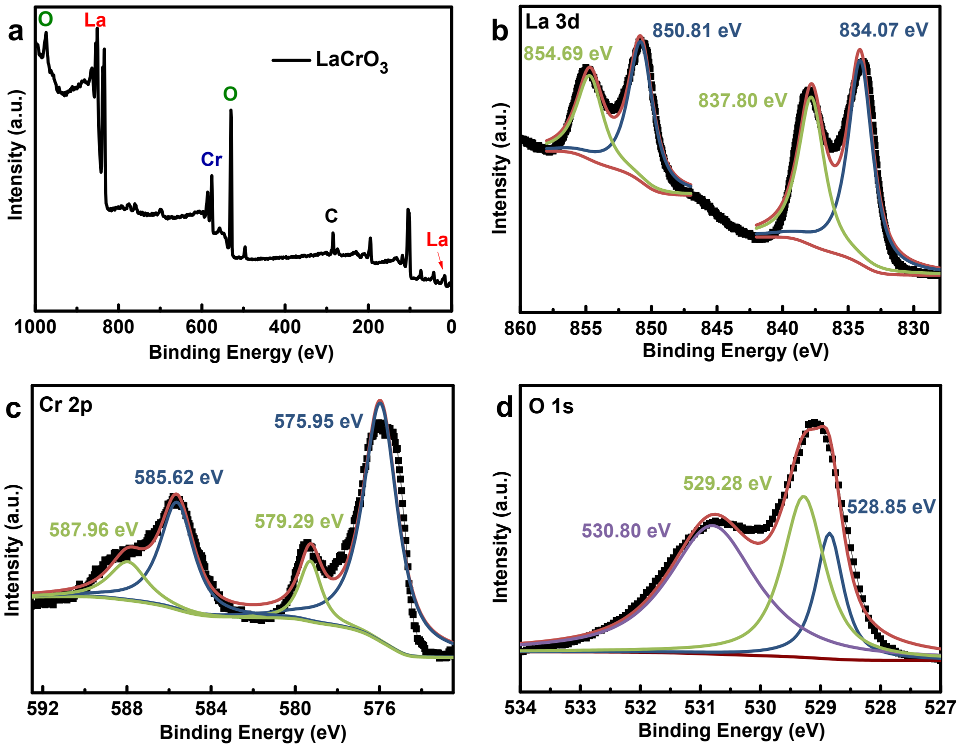

Figure S14. (**a**) Total XPS spectrum, (**b**) La 3d XPS spectrum, (**c**) Cr 2p XPS spectrum, and (**d**) O 1s XPS spectrum of the LaCrO$_3$ sample.

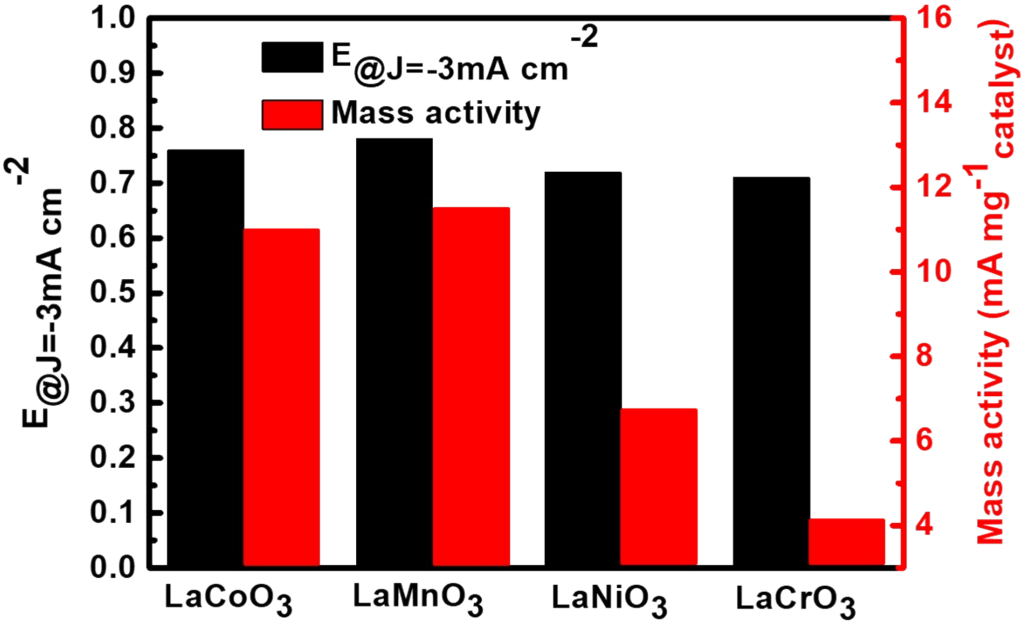

Figure S15. Comparison of $E_{@J=-3\ mA\ cm^{-2}}$ and mass activity at 0.75 V vs. RHE of the $LaCoO_3$, $LaMnO_3$, $LaNiO_3$, and $LaCrO_3$ catalysts in the 0.1 M KOH solution.

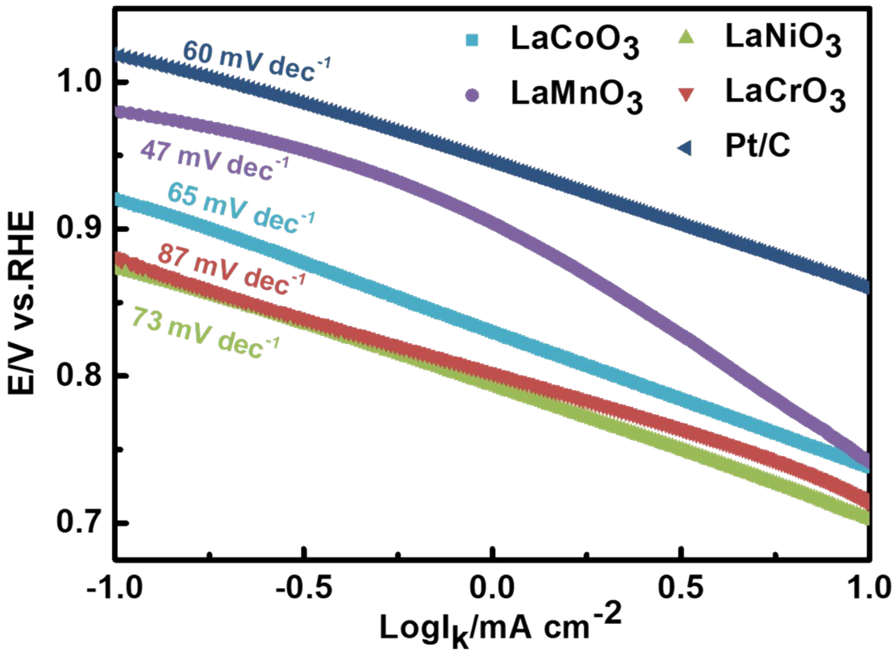

Figure S16. Tafel plots of the $LaCoO_3$, $LaMnO_3$, $LaNiO_3$, $LaCrO_3$, and Pt/C catalysts derived by the mass-transport correction of corresponding LSV data recorded in O_2-saturated 0.1 M KOH at 10 mV s^{-1} and 1600 rpm for ORR. The Tafel slopes of the $LaCoO_3$, $LaMnO_3$, $LaNiO_3$, $LaCrO_3$, and Pt/C catalysts at low overpotential are 65, 47, 73, 87, and 60 mV dec^{-1}, respectively.

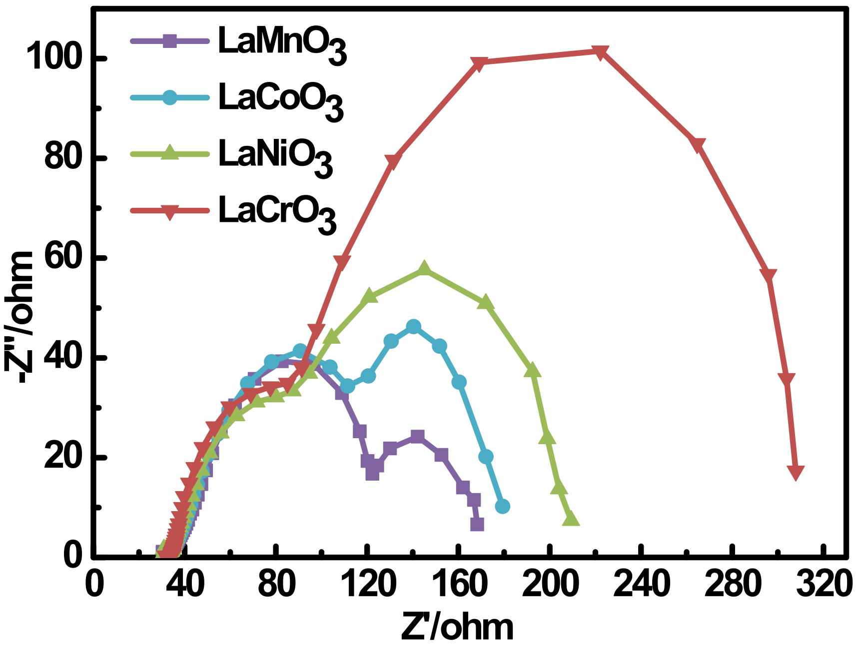

Figure S17. Electrochemical impedance spectra of the $LaCoO_3$, $LaMnO_3$, $LaNiO_3$, and $LaCrO_3$ catalysts at 0.65 V vs. RHE. The impedance responses show two separable semi-circles with comparable information on the electrode processes at high and low frequencies. As Jiang et al.[1] have reported, the observed separable two impedance semi-circles at low and high frequencies show that the O_2 reduction reaction is at least limited by two electrode processes. Takeda et al.[2] reported that the electrode process at the low-frequency semi-circle is most likely a mixed process of dissociative adsorption and diffusion limited by atomic oxygen and molecular oxygen concentration. Jiang et al.[1] reported that the electrode process associated with the high-frequency semi-circle may be the migration and diffusion of oxygen ions from the three-phase boundary and has some characteristics of electrolyte contribution.

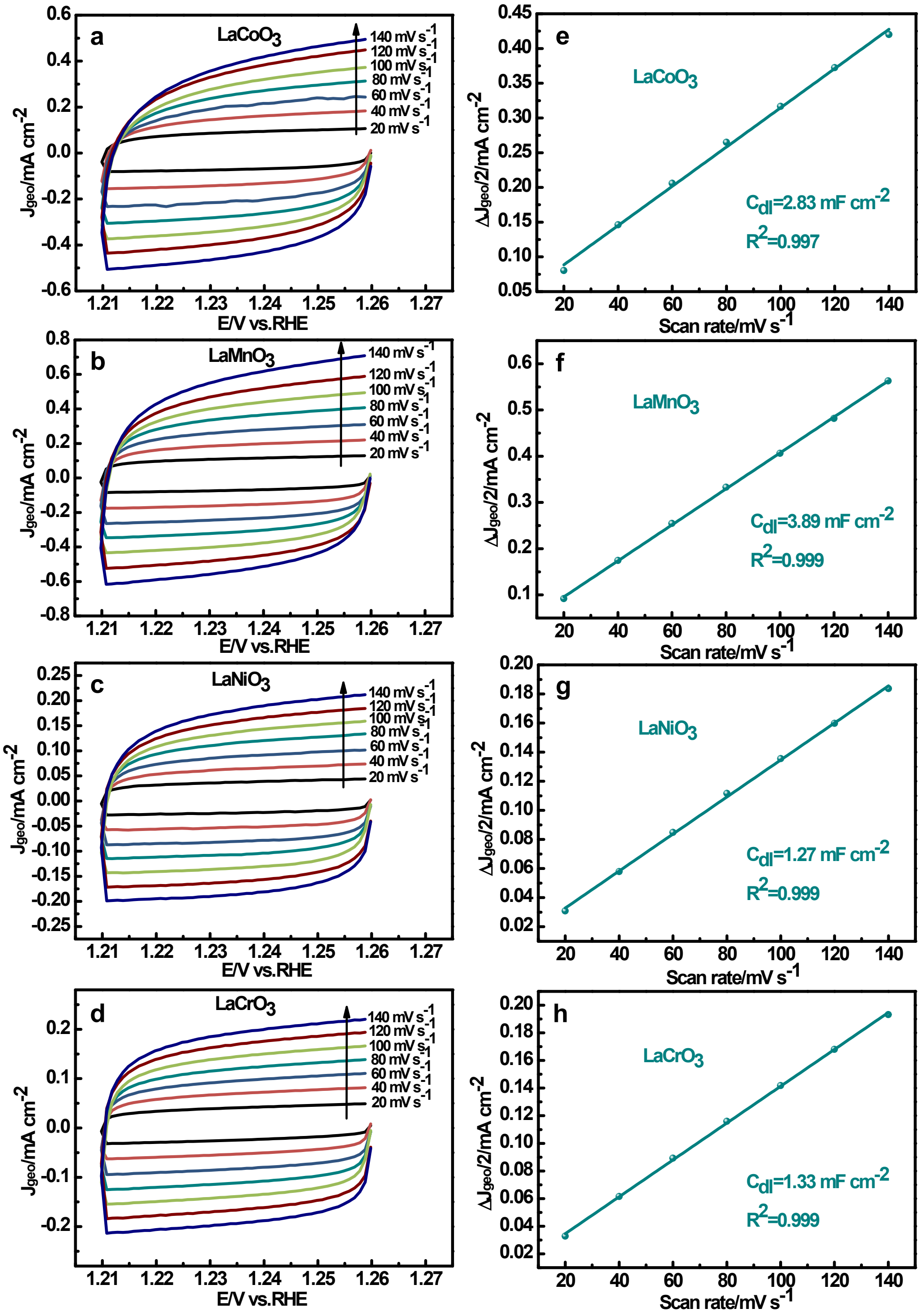

Figure S18. (**a-d**) Electrochemical CV measurements of the (**a**) $LaCoO_3$, (**b**) $LaMnO_3$, (**c**) $LaNiO_3$, and (**d**) $LaCrO_3$ catalysts in 1 M KOH solution at different potential scanning rates from 20 to 140 mV s^{-1}. (**e-h**) Current density differences ($\Delta J_{geo}/2$) of the (**e**) $LaCoO_3$, (**f**) $LaMnO_3$, (**g**) $LaNiO_3$, and (**h**) $LaCrO_3$ catalysts measured at 1.235 V vs. RHE plotted as a function of scan rate.

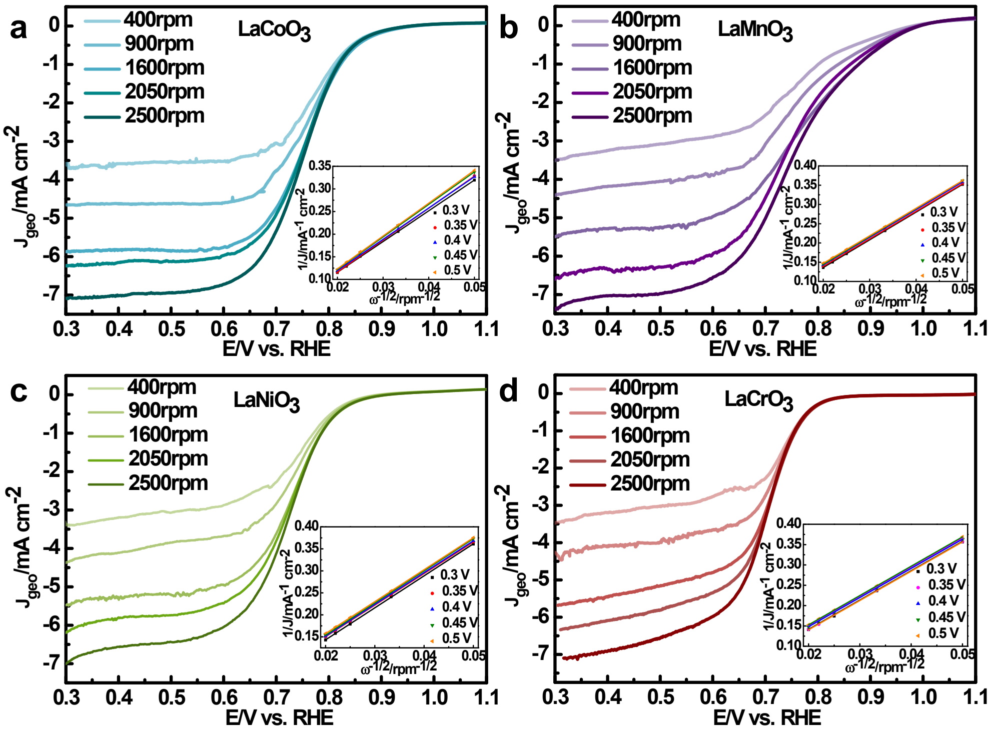

Figure S19. (**a-d**) Polarization curves for ORR on the (**a**) $LaCoO_3$, (**b**) $LaMnO_3$, (**c**) $LaNiO_3$, and (**d**) $LaCrO_3$ catalysts at various rotation rates in the O_2-saturated 0.1 M KOH electrolyte at the scan rate of 10 mV s^{-1}. Insets: Koutecky-Levich plots obtained from the inverse current density (j^{-1}) as a function of the inverse of the square root of the rotation rate ($\omega^{-1/2}$) at different potentials: 0.50, 0.45, 0.40, 0.35, and 0.30 V vs. RHE. The calculated electron transfer numbers for $LaCoO_3$, $LaMnO_3$, $LaNiO_3$, and $LaCrO_3$ are 3.97, 3.93, 3.92, and 3.89, respectively.

The ORR kinetics of the prepared catalyst has been studied with the rotating disk electrode (RDE) measurement. The electron transfer number (*n*) was calculated via the Koutecky-Levich equations:

$$1/J = 1/J_L + 1/J_K = 1/B\omega^{1/2} + 1/J_K$$

$B = 0.62nFkD_0^{2/3}v^{-1/6}C_0$

$J_K = nFkC_0$

in which J, J_K and J_L correspond to the measured current density, the kinetic current density and diffusion-limiting current density respectively, B is a constant as a function of the concentration, diffusion coefficient of O_2 in the electrolyte and viscosity of the electrolyte, F is the Faraday constant (96485 C mol^{-1}), D_0 is the diffusion coefficient of O_2 in the 0.1 M KOH solution (1.9×10^{-5} cm^2 s^{-1}), ω is the angular velocity of the disk (ω=2πN, N is the linear rotation speed), v is the kinetic viscosity of the electrolyte (0.01 cm^2 s^{-1}), C_0 is the bulk concentration of O_2 (1.2×10^{-3} mol cm^{-3}), k is the electron transfer rate constant.

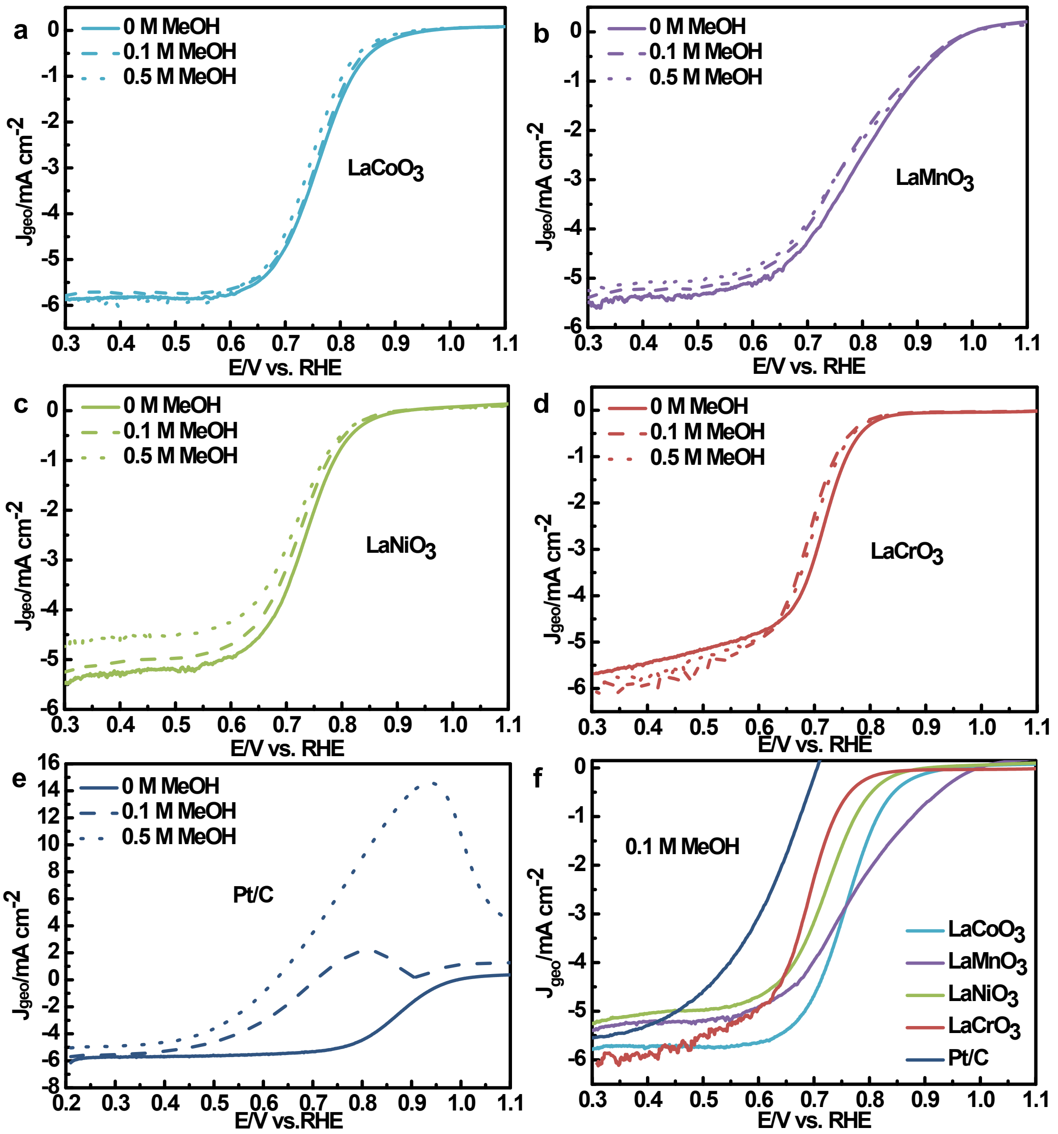

Figure S20. (**a-e**) Polarization curves for ORR on the (**a**) $LaCoO_3$, (**b**) $LaMnO_3$, (**c**) $LaNiO_3$, (**d**) $LaCrO_3$, and (**e**) Pt/C catalysts at the rotation rate of 1600 rpm in the O_2-saturated 0.1 M KOH electrolyte containing 0, 0.1 and 0.5 M MeOH at scan rate of 10 mV s^{-1}. (**f**) Comparison of polarization curves for ORR on the $LaMO_3$ and Pt/C catalysts at a rotation rate of 1600 rpm in the O_2-saturated 0.1 M KOH electrolyte containing 0.1 M MeOH at a scan rate of 10 mV s^{-1}.

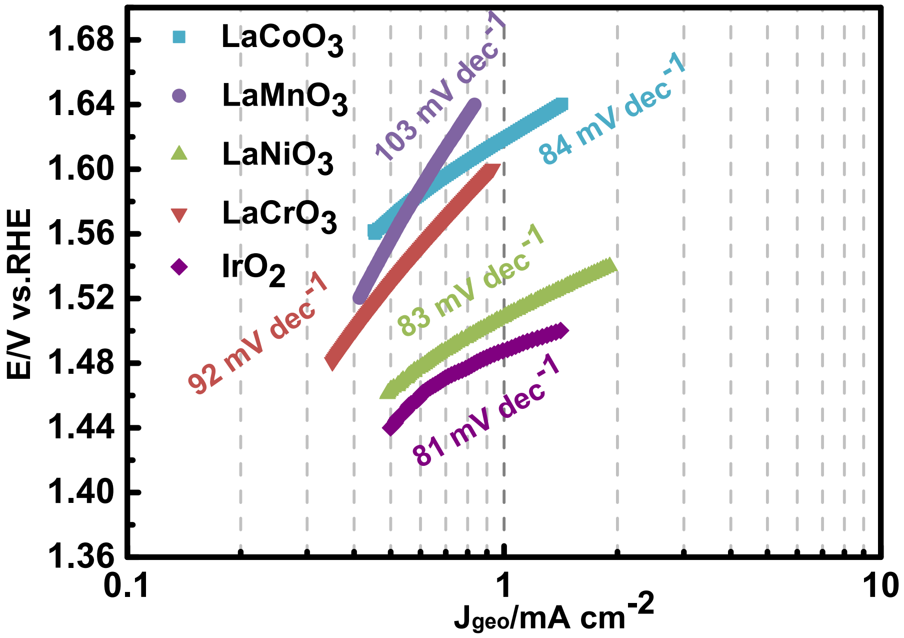

Figure S21. Tafel plots of the $LaCoO_3$, $LaMnO_3$, $LaNiO_3$, $LaCrO_3$, and IrO_2 catalysts for OER. Tafel slopes of the $LaCoO_3$, $LaMnO_3$, $LaNiO_3$, $LaCrO_3$, and IrO_2 catalysts are 84, 103, 83, 92, and 81 mV dec^{-1}, respectively.

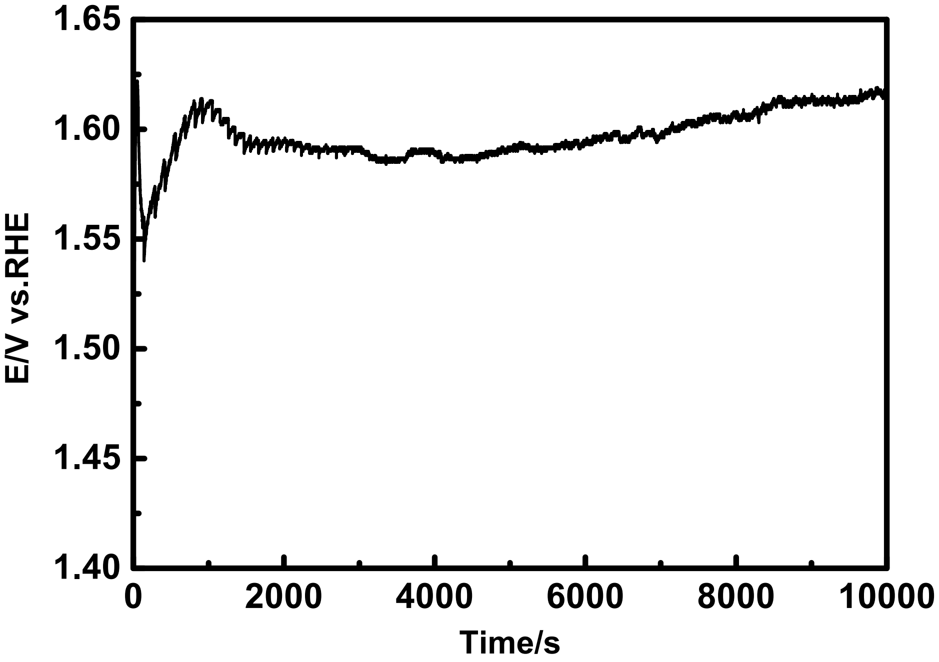

Figure S22. Chronopotentiometry curves of $LaNiO_3$ at a constant current density of 10 mA cm^{-2} in 1 M KOH.

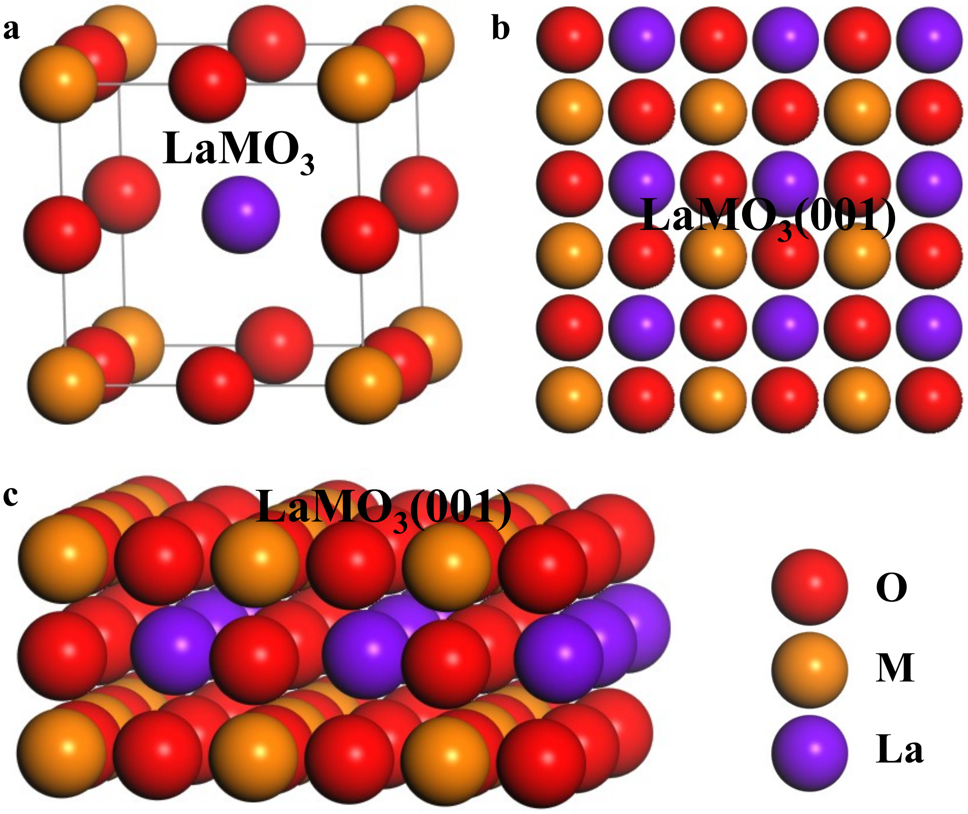

Figure S23. (**a**) The structure of the bulk perovskite-type $LaMO_3$ (M = Co, Mn, Ni, or Cr). (**b**) Top view of the $LaMO_3$ (001) structure. (**c**) Side view of the $LaMO_3$ (001) structure.

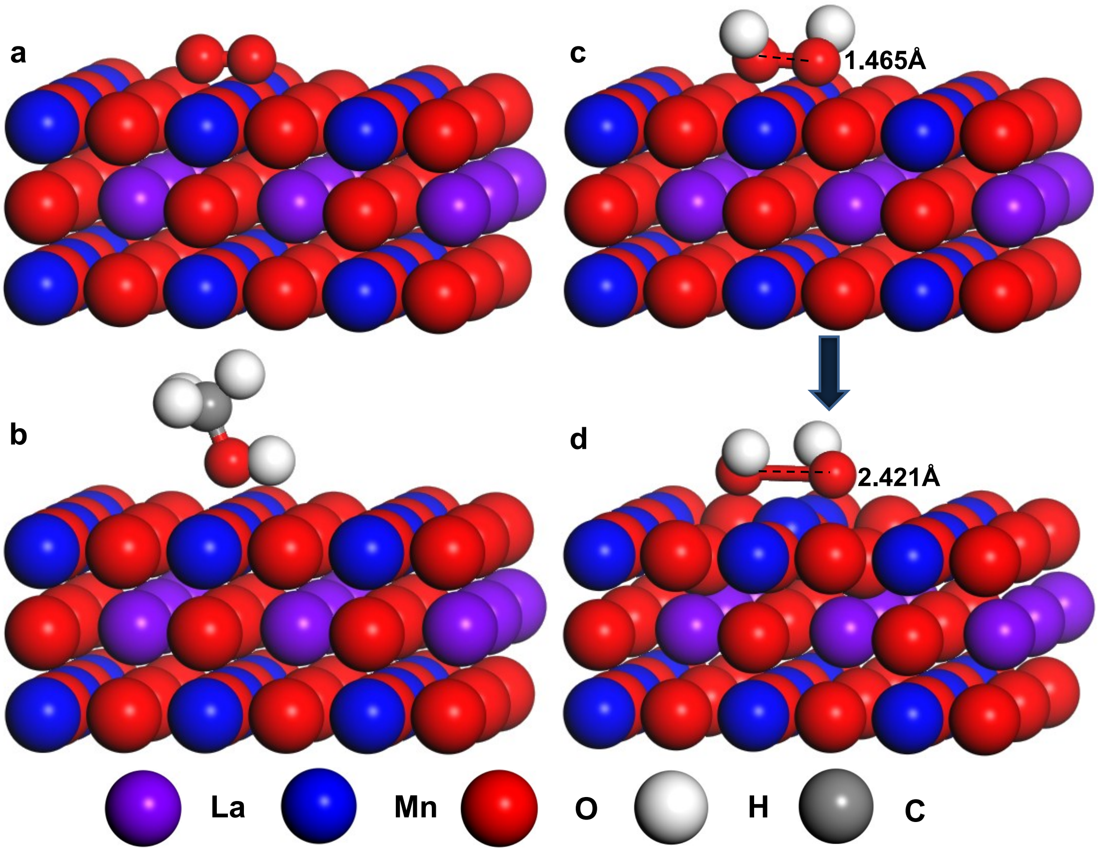

Figure S24. (**a**) The status of O_2 molecule adsorbed on the $LaMnO_3$ (001). (**b**) The status of CH_3OH molecule adsorbed on the $LaMnO_3$ (001). (**c,d**) The status of HOOH molecules adsorbed on the $LaMnO_3$ (001) (**c**) before and (**d**) after optimization.

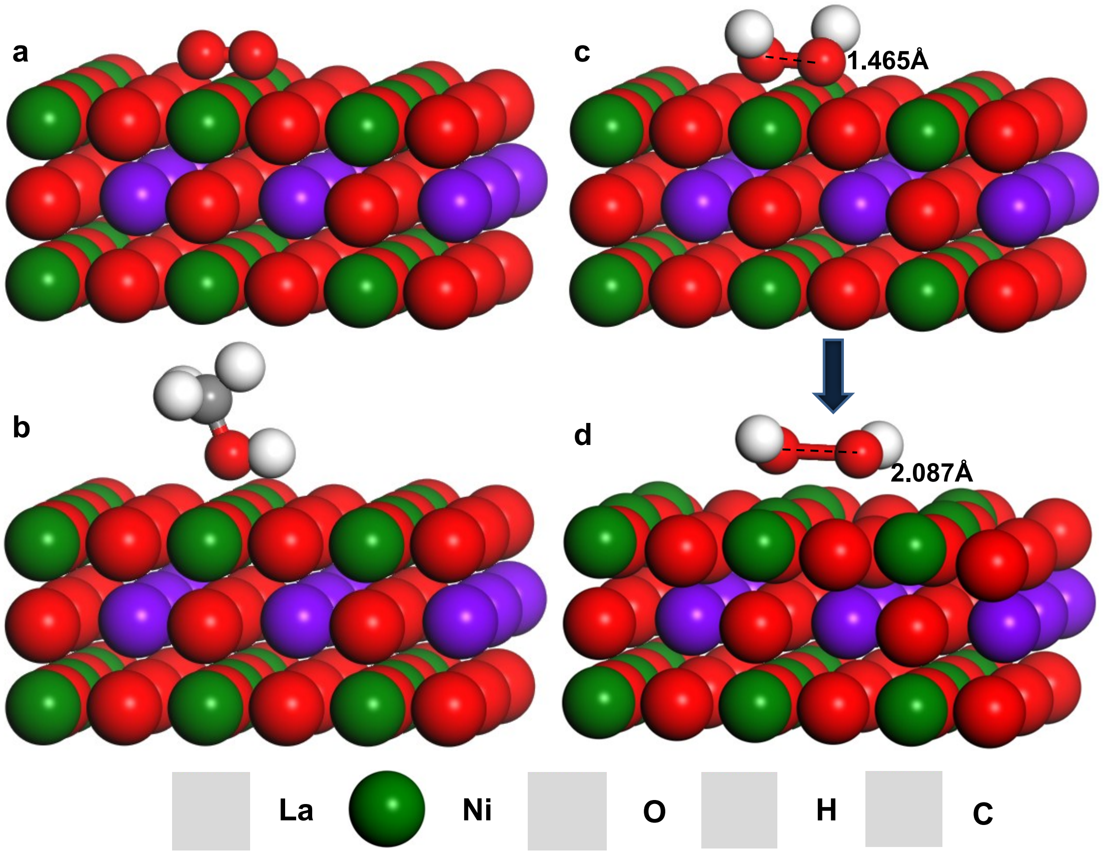

Figure S25. (**a**) The status of O_2 molecule adsorbed on the $LaNiO_3$ (001). (**b**) The status of CH_3OH molecule adsorbed on the $LaNiO_3$ (001). (**c,d**) The status of HOOH molecules adsorbed on the $LaNiO_3$ (001) (**c**) before and (**d**) after optimization.

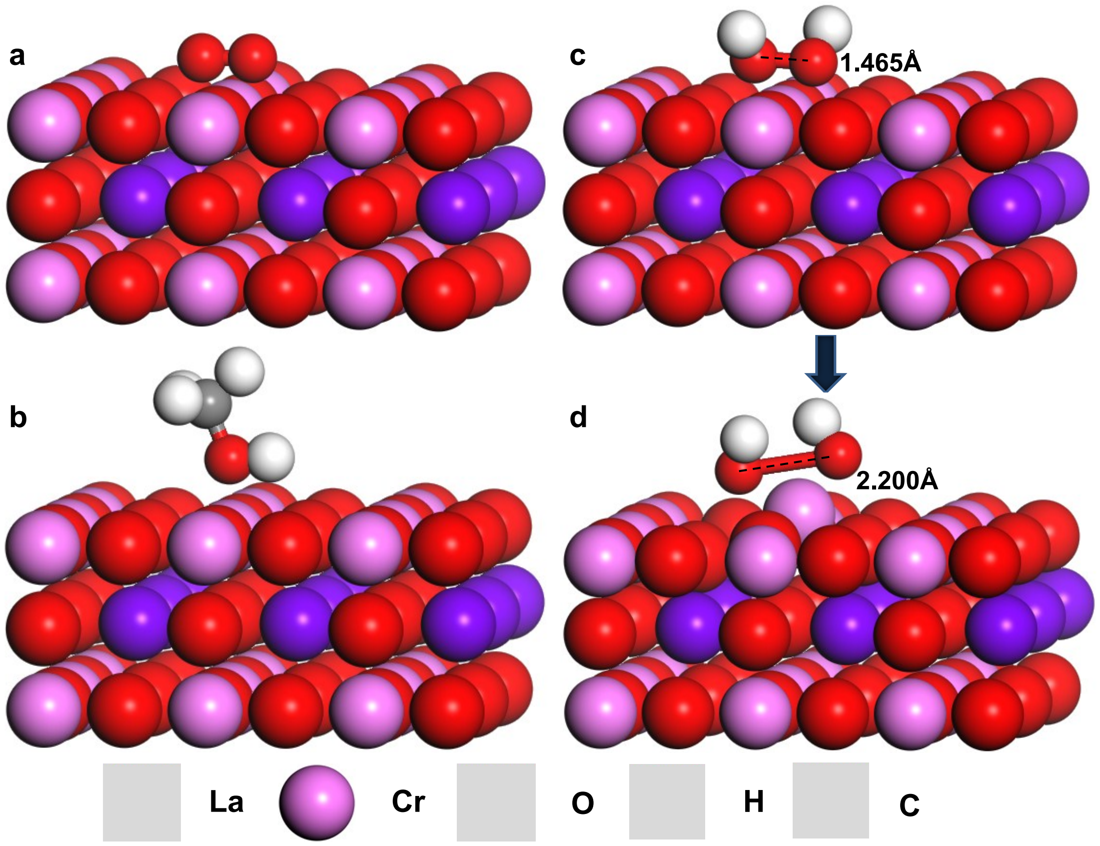

Figure S26. (**a**) The status of O_2 molecule adsorbed on the $LaCrO_3$ (001). (**b**) The status of CH_3OH molecule adsorbed on the $LaCrO_3$ (001). (**c,d**) The status of HOOH molecules adsorbed on the $LaCrO_3$ (001) (**c**) before and (**d**) after optimization.

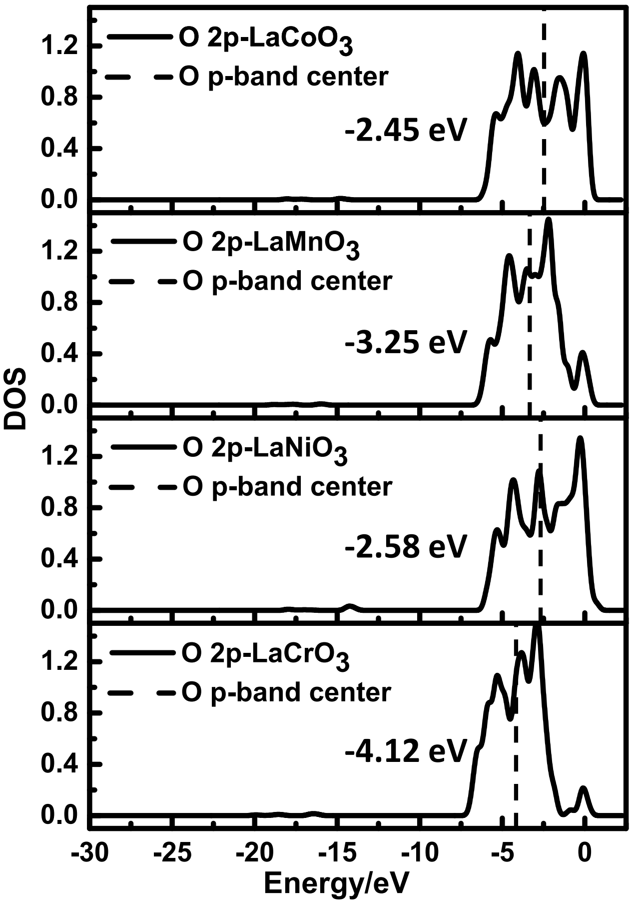

Figure S27. The O 2p DOS of $LaCoO_3$, $LaMnO_3$, $LaNiO_3$, and $LaCrO_3$. The O p-band centers of $LaCoO_3$, $LaMnO_3$, $LaNiO_3$, and $LaCrO_3$ are at -2.45, -3.25, -2.58, and -4.12 eV, respectively.

Supplementary Tables

Table S1. The relative ratios of peak area for various oxygen species of the $LaCoO_3$ and $LaMnO_3$ samples obtained from the XPS results **(Fig. 2h** and **Fig. S12d).**

O - $LaCoO_3$		**O - $LaMnO_3$**		**Representative object**
Position (eV)	Area (%)	Position (eV)	Area (%)	—
528.91	22.96	529.28	19.54	O^{2-}
531.69	62.58	531.73	58.26	$-OH/O_2$
533.16	14.46	533.16	22.20	H_2O/OH^-

Table S2. Comparison of ORR results for the $LaCoO_3$, $LaMnO_3$, $LaNiO_3$, and $LaCrO_3$ catalysts.

	$\mathbf{LaCoO_3}$	$\mathbf{LaMnO_3}$	$\mathbf{LaNiO_3}$	$\mathbf{LaCrO_3}$
Onset potential (V vs. RHE)	0.96	1.00	0.86	0.84
Limiting current density (mA cm^{-2}_{geo})	5.87	5.53	5.46	5.65
$E_{@J=-3mA\ cm}{}^{-2}$ (V vs. RHE)	0.76	0.78	0.72	0.71
$J_{@E=0.75V}$ (mA cm^{-2}_{geo})	3.30	3.45	2.02	1.24
Mass activity$_{@E=0.75V}$ (mA $mg^{-1}_{catalyst}$)	11.00	11.50	6.73	4.13
Tafel slope at low overpotential (mV dec^{-1}) for ORR	65	47	73	87
Transferred electron number (n) from the Koutecky-Levich equations	3.97	3.93	3.92	3.89
Transferred electron number (n) from the RRDE data	3.93-3.99	3.90-3.95	3.87-3.98	3.83-3.92

Table S3. Comparison of ORR parameters of the $LaMO_3$ (M = Co, Mn, Ni, or Cr) catalysts with the active perovskite electrocatalysts in the literatures.[3-12]

Catalyst	Onset potential (V vs. RHE)	Limiting current density (mA cm^{-2})$_{geo}$	$E_{@J=-3\ mA\ cm-2}$ (V vs. RHE)	Specific surface area (m^2 g^{-1})	Rotation rate (rpm)	Loading catalyst (mg cm^{-2})	Electrolyte solution	Ref.
$LaCoO_3$	**0.96**	**5.87**	**0.76**	**9.25**	**1600**	**0.30**	**0.1 M KOH**	**This work**
$LaMnO_3$	**1.00**	**5.53**	**0.78**	**20.13**	**1600**	**0.30**	**0.1 M KOH**	**This work**
$LaNiO_3$	**0.86**	**5.46**	**0.72**	**11.75**	**1600**	**0.30**	**0.1 M KOH**	**This work**
$LaCrO_3$	**0.84**	**5.65**	**0.71**	**8.10**	**1600**	**0.30**	**0.1 M KOH**	**This work**
$La_{0.7}(Ba_{0.5}Sr_{0.5})_{0.3}Co_{0.8}Fe_{0.2}O_{3-\delta}$	0.76	5.60	0.64	4.20	1600	0.64	0.1 M KOH	[3]
$LaNiO_3$-NR/RGO	0.67	4.65	0.54	---	1600	0.25	0.1 M KOH	[4]
$LaMnO_3$/RGO	0.77	3.52	0.43	---	1600	0.25	0.1 M KOH	[5]
$La_{1-x}Sr_xCrO_3$-H	0.81	5.64	0.68	---	1600	0.26	0.1 M KOH	[6]
$LaFe_{0.95}Pd_{0.05}O_{3-\delta}$	0.78	4.90	0.62	---	1600	0.23	0.1 M KOH	[7]
$La_{0.95}FeO_{3-\delta}$	0.68	2.90	---	6.48	1600	0.46	0.1 M KOH	[8]
$LaCu_{0.5}Mn_{0.5}O_3$	0.80	5.65	0.63	---	1600	0.25	0.1 M KOH	[9]
$La_{0.6}Ca_{0.4}MnO_3$-graphene	0.77	3.55	0.40	---	1600	0.06	0.1 M KOH	[10]
$La_{0.8}Sr_{0.2}MnO_3$	0.75	5.10	0.57	48.00	2500	0.66	0.1 M KOH	[11]
$La_{0.8}Sr_{0.2}Co_{0.4}Mn_{0.6}O_3$	0.88	5.70	0.71	9.90	1600	0.26	0.1 M KOH	[12]

Table S4. Comparison of OER parameters of the $LaNiO_3$ catalyst with the active perovskite electrocatalysts in the literatures.[11-17]

Catalyst	Onset potential (V vs. RHE)	$E_{J=10\ mA\ cm^{-2}}$ (V vs. RHE)	Specific surface area	Electrolyte solution	Ref.
$LaNiO_3$	**1.45**	**1.60**	**11.75**	**1 M KOH**	**This work**
$La_{0.8}Sr_{0.2}MnO_3$	1.47	---	48.00	0.1 M KOH	[11]
$La_{0.8}Sr_{0.2}Co_{0.4}Mn_{0.6}O_3$	1.50	1.74	9.90	0.1 M KOH	[12]
$LaNi_{0.85}Mg_{0.15}O_3$	1.63	1.85	---	0.1 M KOH	[13]
$LaNiO_3$	1.59	1.80	25.00	0.1 M KOH	[14]
$LaNiO_3$/CNT	1.55	1.61	---	0.1 M KOH	[15]
NiO-$(La_{0.613}Ca_{0.387})_2NiO_{3.562}$	1.55	1.62	10.80	0.1 M KOH	[16]
$LaNiO_3$	1.67	2.09	---	0.1 M KOH	[17]

Table S5. Comparison of d-band center and molecular adsorption results for $LaCoO_3$ (001), $LaMnO_3$ (001), $LaNiO_3$ (001), and $LaCrO_3$ (001) (corresponding to the optimized structural configurations in **Fig. 4** and **Fig. S24-26**).

	$LaCoO_3$ (001)	**$LaMnO_3$ (001)**	**$LaNiO_3$ (001)**	**$LaCrO_3$ (001)**
d-band center (eV)	-1.52	-1.47	-1.97	-1.30
O_2 adsorption energy (eV)	3.09	2.17	1.59	3.02
CH_3OH adsorption energy (eV)	0.15	0.26	0.21	0.19
O-O bond length change of HOOH (**Å**)	1.465→2.232	1.465→2.421	1.465→2.087	1.465→2.200

Notes and references

1. S.P. Jianga, J.G. Love and Y. Ramprakash, *J. Power Sources*, 2002, **110**, 201-208.
2. Y. Takeda, R. Kanno, M. Noda, Y. Tomida and O. Yamamoto, *J. Electrochem. Soc.*, 1987, **134**, 2656-2661.
3. J. Jung, M. Risch, S. Park, M. G. Kim, G. Nam, H. Y. Jeong, Y. S. Horn and J. Cho, *Energy Environ. Sci.*, 2016, **9**, 176-183.
4. J. Hu, Q. Liu, Z. Shi, L. Zhang and H. Huang, *RSC Adv.*, 2016, **6**, 86386-86394.
5. J. Hu, L. Shi, Q. Liu, H. Huang and T. Jiao, *RSC Adv.*, 2015, **5**, 92096-92106.
6. B. H. Choi, S. A. Park, B. K. Park, H. H. Chun and Y. T. Kim, *Mater. Res. Bull.*, 2013, **48**, 3651-3656.
7. Y. Zhu, W. Zhou, Y. Chen, J. Yu, X. Xu, C. Su, M. O. Tadé and Z. Shao, *Chem. Mater.*, 2015, **27**, 3048-3054.
8. Y. Zhu, W. Zhou, J. Yu, Y. Chen, M. Liu and Z. Shao, *Chem. Mater.***,** 2016, **28**, 1691**-**1697.
9. J. Suntivich, H. A. Gasteiger, N. Yabuuchi, H. Nakanishi, J. B. Goodenough and Y. S. Horn, *Nat. Chem.*, 2011, **3**, 546-550.
10. J. Hu, L. Wang, L. Shi and H. Huang, *J. Power Sources*, 2014, **269**, 144-151.
11. C. Jin, X. Cao, L. Zhang, C. Zhang and R. Yang, *J. Power Sources*, 2013, **241**, 225-230.
12. Q. Wang, Y. Xue, S. Sun, S. Li, H. Miao and Z. Liu, *Electrochim. Acta*, 2017, **254**, 14-24.
13. Z. Du, P. Yang, L. Wang, Y. Lu, J. B. Goodenough, J. Zhang and D. Zhang, *J. Power Sources*, 2014, **265**, 91-96.
14. C. L. McBean, H. Liu, M. E. Scofield, L. Li, L. Wang, A. Bernstein and S. S. Wong, *ACS Appl. Mater. Interfaces*, 2017, **9**, 24634-24648.
15. C. T. Alexander, A. M. Abakumov, R. P. Forslund, K. P. Johnston and K. J. Stevenson, *ACS Appl. Energy Mater.*, 2018, **1**, 1549-1558.
16. R. Liu, F. Liang, W. Zhou, Y. Yang and Z. Zhu, *Nano Energy*, 2015, **12**, 115-122.
17. Y. Wu, T. Wang, Y. Zhang, S. Xin, X. He, D. Zhang and J. Shui, *Sci. Rep.*, 2016,

6, 24314.